Eur. Phys. J. B (2013) 86: 118
DOI: 10.1140/epjb/e2013-30778-y

THE EUROPEAN PHYSICAL JOURNAL B

Regular Article

Self-interstitial clusters in radiation damage accumulation: coupled molecular dynamics and metadynamics simulations

Paul R. Monasterio[1,a], Sidney Yip[1,2,b], and Bilge Yildiz[1,c]

[1] Department of Nuclear Science and Engineering, Massachusetts Institute of Technology, Cambridge, MA 02139, USA
[2] Department of Materials Science and Engineering, Massachusetts Institute of Technology, Cambridge, MA 02139, USA

Received 26 August 2012 / Received in final form 20 January 2013
Published online 27 March 2013 –

Abstract. Self-interstitial interactions causing volume expansion in bcc Fe are studied through an idealized microstructure evolution model in which only self-interstial atoms (SIAs) are inserted. Using a combination of non-equilibrium molecular dynamics simulations and a metadynamics algorithm, meta-stable SIA clusters are observed to nucleate and grow into dislocation loops or localized amorphous phases, both contributing to swelling behavior persisting well beyond the atomistic time scale. A non-monotonic local density variation with dose rate is found and attributed to competing evolutions of different defective structures.

1 Introduction

Irradiation of metals leads to dramatic microstructural changes as a result of atom displacements of lattice atoms and energy deposition via electronic and ionic excitations [1,2]. At the macroscale these include dimensional instabilities such as creep, growth, shrinkage, and swelling [1,3]. Irradiation creep and growth are volume-conserving shape-modifying processes enhanced by the induced microstructural changes. Swelling, on the other hand, involves volume increases caused by the formation and growth of voids, the retention of lattice vacancies, or the development of less dense phases [1], all of which can result from the formation and evolution of Frenkel pairs produced during displacement cascades and their subsequent interactions with the evolving metallic microstructure.

Irradiated crystalline metals are characterized by super-saturation of both vacancies and self-interstitial atoms (SIA) generated during displacement cascades. Though a large fraction of the defects generated recombine after a few picoseconds, the concentrations of both vacancies and SIAs left behind are still orders of magnitude higher than those in the unirradiated metal. In contrast to the role of vacancies and voids in swelling which has been thoroughly studied [4–6], the role of self-interstitials in causing volumetric expansion is still not well understood. At high dose rates, low total doses, or low temperatures, void nucleation and growth are unlikely to be responsible for dimensional changes in the material because the migration barrier for free vacancies in Fe is on the order of 0.5–0.6 eV [7], and the low point defect concentrations make it difficult for vacancies to migrate sufficiently to coalesce. However, SIAs are known to migrate rapidly and distort the local microstructure appreciably. For example, amorphization of crystalline materials has been observed under electron and ion-beam bombardment [8,9] and described as self-interstitial driven disorder rather than vacancy-mediated effects [10]. This amorphization process can lead to low density disordered phases which then result in swelling enhancement at high irradiation doses. The formation of such disordered phases in a variety of lattices is known to depend strongly on total irradiation dose and dose rate, with aggressive irradiation conditions necessary for full destabilization [9,10]. Furthermore, the strong long-range interaction between self-interstitial atoms (SIA) [8] and low energy recoils from primary knock-on atoms [9,11] are known to result in strong driving forces for athermal recrystallization in competition with formation and growth of disordered phases, both having important effects on macroscopic volumetric instabilities.

The purpose of this work is to characterize the mechanisms by which SIAs contribute to volumetric instabilities in Fe under extreme irradiation conditions. We employ non-equilibrium molecular dynamics (MD) simulations and a constant pressure version of an activation-relaxation method of sampling transition state pathways, hereafter denoted as the autonomous basin climbing (ABC) method [12–14], to probe the microstructural changes resulting from self-interstitial insertion in a body-centered cubic (bcc) Fe lattice. As we will see, these changes include the formation, growth, agglomeration, and recovery of disordered phases leading to swelling which persists

[a] e-mail: paul.monasterio@gmail.com
[b] e-mail: syip@mit.edu
[c] e-mail: byildiz@mit.edu

beyond the atomistic scale. Section 2 describes the details of the MD simulations and simplifications associated with the self-interstitial insertion methodology as well as the isobaric ABC methodology for the study of post-irradiation evolution at time scales not accessible by MD simulations. Section 3 presents the main macroscopic results highlighting the volume overexpansion, which results from self-interstitial insertion. Section 4 addresses the geometrical changes in the crystalline microstructure and the corresponding atomistic mechanisms which give rise to swelling under different irradiation conditions. Section 5 summarizes the paper and describes future steps to extend our approach with additional generalizations of the ABC method.

2 Self-interstitial insertion and simulation methodology

Non-equilibrium MD simulations were performed in a $10 \times 10 \times 10$ bcc Fe super-cell (2000 atoms) with periodic boundary conditions. We use the recent Fe interatomic potential developed by Ackland et al. [15], which appropriately describes the properties of both crystalline and highly disordered phases essential in our study. The choice of a bcc, rather than fcc, phase of Fe is intentional, as experimental observations [16] indicate that void swelling is significantly lower in the bcc phase, and therefore the effect of SIAs should be more relevant for bcc Fe. All MD simulations are performed at a constant temperature of 400 K and zero external pressure. Irradiation conditions are simulated by randomly introducing one or more Fe atoms in octahedral or tetrahedral interstitial sites relative to the existing atoms in the lattice. The atoms are introduced with equal probability at equal intervals after a fixed number of time steps. While this procedure is a simplification of the realistic (more complex) recombination dynamics, it is easy to implement and the effects are simple to interpret. In our study each inserted atom is counted as a lattice displacement and therefore the corresponding dose associated with each insertion is given by:

$$dpa_{insertion}(t) = \frac{n}{N(t)}, \tag{1}$$

where $N(t)$ is the total number of atoms in the simulation cell at the time of insertion t and n is the number of atoms inserted at time t. The total dose is obtained by adding the doses of all insertions, and the average dose rate is given by dividing the total dose by the time interval of irradiation. Irradiation conditions for all the simulation runs are given in Table 1 below. Although the dose rates explored, ranging from 5×10^7 to 7×10^9 dpa/s, are higher than current reactor or ion beam applications, we expect the results will still provide qualitative and systematic insights into the defect formation mechanisms associated with SIA-induced damage and swelling. Previous simulations of radiation induced amorphization using similar simplifications [17] and considering both vacancies and interstitials have produced similar results to those using self-interstitial insertion only while requiring higher total doses and higher dose rates because of recombination.

In addition to the non-equilibrium MD simulations, we have probed the evolution of the system after irradiation at longer time scales by using a constant stress extension of the ABC method [12,14]. For this part of our study, designed to sample relaxation processes on a time scale longer than the volumetric relaxation probed by MD, we add a cell relaxation step during the minimization procedure immediately after the jump to a new energy minimum on the potential energy surface. In this algorithm, a fixed cell volume is chosen and then the steps of the microcanonical ABC algorithm (at a constant volume V) [12] are followed until a new minimum and saddle point are found. More precisely, we consider an initial microstate which is relaxed to a local minimum configuration $Q^{(1)}_{\min} = (q_1^{\min}, \ldots, q_N^{\min})$ by using standard energy minimization procedures such as conjugate gradient, where $q_1^{\min}, \ldots, q_N^{\min}$ are the Cartesian positions of the atoms in the lattice. This configuration has a corresponding energy $E^{(1)}_{\min} = \Phi(Q^{(1)}_{\min})$, where Φ is the potential describing the interparticle interactions. The system is then driven away from this configuration by imposing Gaussian penalty functions to the potential energy, which result in fictitious forces which move the system away from the original minimum configuration basin [18,19]. Gaussian penalty functions are imposed on fractional, rather than Cartesian, coordinates such that:

$$\varphi_i(s) = W \exp\left(-\frac{\left(Hs - Hs^{(i)}_{\min}\right)^2}{2\left(\sigma\left(\frac{V}{V_o}\right)^{1/3}\right)^2} \right) \tag{2}$$

where φ_i is the ith Gaussian penalty function, W and σ are the corresponding Gaussian height and width parameters, s and $s^{(i)}_{\min}$ are the positions of the microstate in fractional coordinates corresponding to the current state and the local minimum energy configuration after i penalties have been added, H is the matrix defining the shape of the unit cell at the given time step, and V and V_o are the volumes of the unit cell at the current and initial time steps. After the local minimum configuration is found, the cell shape is relaxed and particle positions are allowed to converge to a new minimum. The cell relaxation step takes place at a temperature of $T = 0$ K. A fictitious pressure, taken as the equilibrium average after the initial relaxation at $T = 400$ K, is included to account for the thermal stresses. After a local equilibrium volume is found, the pressure is calculated by averaging over a virial expression, the atomic configuration is quenched at a fixed volume, more penalty functions are added, and the evolution continues. The total (penalized) system potential energy then becomes $\Phi^1_p = \Phi + \sum_i \phi_i$. The system configuration is relaxed under the new penalized potential energy landscape until it reaches a new configuration $Q^{(2)}_{\min}$ with corresponding potential energy $E^{(2)}_{\min}$. The minimization path is backtracked until a saddle point separating the two minima is identified, corresponding to a

Table 1. Irradiation conditions for the MD simulations.

Simulation run	Total number of inserted atoms	Irradiation time (s)	Total dose (mdpa)	Average dose rate (dpa/s)
1	75	7.60×10^{-10}	37.0	4.84×10^{7}
2	75	4.50×10^{-10}	37.0	8.18×10^{7}
3	75	2.25×10^{-10}	37.0	1.64×10^{8}
4	75	1.12×10^{-10}	37.0	3.27×10^{8}
5	75	2.25×10^{-11}	37.0	1.64×10^{9}
6	200	3.00×10^{-11}	95.0	3.18×10^{9}
7	200	1.50×10^{-11}	95.0	6.36×10^{9}

configuration $Q_{\mathrm{sad}}^{(12)}$ with energy $E_{\mathrm{sad}}^{(12)}$. The procedure is then iterated to obtain a sequence of minimum and saddle point energies describing the topology of the underlying energy landscape. The need to penalize in fractional coordinates and to maintain Gaussian penalties even after the cell is relaxed results from the fact that the energy barriers that must be overcome to change the cell volume are small. This implies that the system can return to an already visited basin via a slightly different chain of cell shape changes if the Gaussians are removed, greatly reducing the efficiency of the algorithm. The parameters for the penalty function are scaled dynamically since the size of the phase space sampled is volume-dependent and each given basin grows with the cell volume.

The ABC constant pressure runs start immediately after irradiation was completed. For improved statistical accuracy, multiple MD simulations with different initial configurations for each of the conditions described in Table 1 were performed until the integral properties converged. Unless otherwise noted, the results presented below represent averages over these simulations.

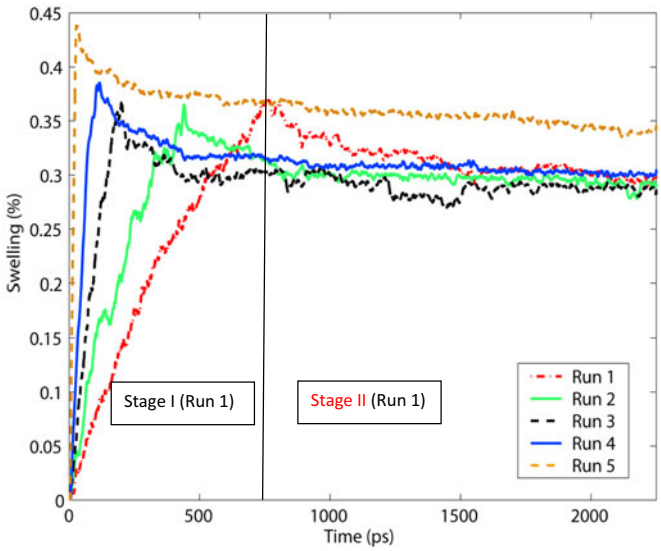

Fig. 1. Swelling, as measured by the normalized inverse density, as a function of time for various dose rates (runs 1–5). In all cases, the total dose is 37 mdpa and the total simulated time is 2.25 ns. Stage I (irradiation) finishes at the peak of maximum swelling for each of the runs, at which point stage II (recovery) begins.

3 Macroscopic effects: self-interstitial induced swelling

Figure 1 and part of Figure 2 summarize the macroscopic effects of SIA insertion rate in a bcc Fe lattice for runs 1 through 5, all with a total dose of 37 mdpa, but with varying dose rates. Since the number of lattice atoms in the system increases during irradiation, the volume of the material increases to accommodate the increased stresses. Figure 1 quantifies this volumetric expansion by using the normalized inverse density ($v_{normalized}$), a measure of the swelling per atom. $v_{normalized}$ was obtained from MD simulations up to 2.25 ns, and is defined as follows:

$$v_{normalized}\,(t) = \frac{V(t)N(0)}{V(0)N(t)} - 1, \qquad (3)$$

where $V(t)$ and $N(t)$ are the volume and number of atoms of the lattice at time t. Figure 2 summarizes the swelling behavior for runs 4 through 7. Table 2 summarizes the resulting swelling levels right after irradiation, and in the short (2.25 ns) and the long runs following irradiation for all the conditions given in Table 1. Figure 1 demonstrates that irradiation, under the aggressive conditions studied in this work, results in an overexpansion of the volume in excess of the relaxation required to accommodate the increased number of atoms in the lattice. At the end of our 2.25 ns simulations, this excess swelling, as measured by $v_{normalized}$, varies over a small range from 0.28% for run 3 to 0.34% for run 5 in the range of dose rates explored for a total dose of 37 mdpa. This in turn corresponds to a swelling rate of approximately 7.7–8.7% /dpa, which is a factor of 8 larger than the ∼1.0% /dpa observed experimentally in nuclear reactor steels [20]. However, reactor irradiation conditions involve dose rates which are orders of magnitude lower than in our simulations, and in this low dose rate regime the swelling behavior is believed to be dominated by vacancy-driven processes such as void nucleation and growth [4,6] instead of SIA-driven processes. Our calculations – occurring in a high dose rate regime and indicating important effects of SIAs in the swelling process – would be relevant for more aggressive conditions such as ion implantation.

As one can see in Figure 1 and Table 2, the effects of dose rate on total swelling in the range of conditions studied indicate an interesting trend. Immediately after irradiation the variance in $v_{normalized}$, is quite large. These far-from-equilibrium effects relax away on a scale of a

Table 2. Short and long-term swelling at various dose and dose rates. Long time scale results are obtained from the ABC simulations with the associated time scales described in Section 3.

Simulation run	Total dose (mdpa)	Average dose rate (dpa/s)	Swelling after irradiation (%)	Swelling at $t = 2.25$ ns (%)	Swelling at $t \gg 1$ year (%)
1	37.0	4.84×10^7	0.37	0.30	0.29
2	37.0	8.18×10^7	0.35	0.29	0.29
3	37.0	1.64×10^8	0.33	0.28	0.28
4	37.0	3.27×10^8	0.38	0.30	0.29
5	37.0	1.64×10^9	0.44	0.34	0.33
6	95.0	3.18×10^9	0.78	0.42	0.40
7	95.0	6.36×10^9	0.80	0.39	0.38

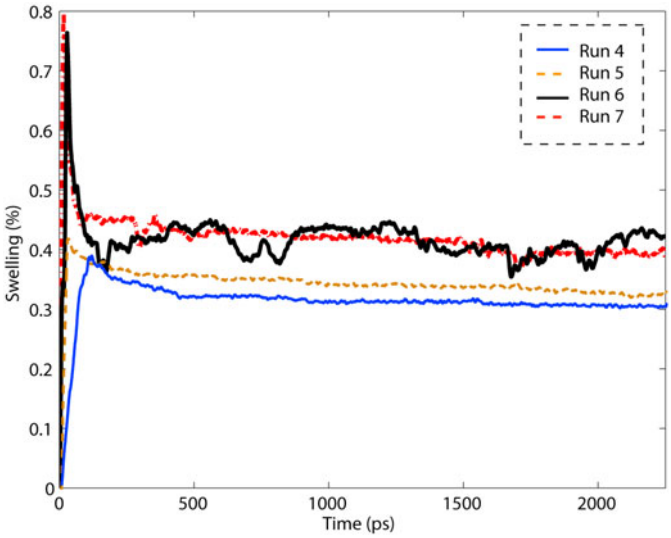

Fig. 2. Swelling, as measured by the normalized inverse density, as a function of time for various irradiation conditions (runs 4–7). The total simulated time is 2.25 ns.

few nanoseconds. From the apparently converged swelling levels one can see that minimum swelling occurs at intermediate dose rates (such as in run 3) rather than at the low or high (such as runs 1 and 5, respectively) dose rates. This non-monotonic behavior is somewhat unexpected. As discussed below we believe it points to an interesting interplay between the different defect microstructures and their evolutions.

As one can see in runs 5 and 6 in Figure 2, for similar irradiation dose rates, the swelling levels immediately after irradiation are primarily determined by the total dose. Significant recovery takes place within a few nanoseconds and the swelling at higher doses decreases sharply, recovering over 50% of the swelling within picoseconds. This is similar to the type of fast recovery observed during the introduction of displacement cascades. In that instance the recovery is the result of recombination of Frenkel pairs. In the present case in which no vacancies are introduced, a different mechanism of recovery is found to operate.

The microstructural evolution at long times, probed with ABC (constant pressure) simulations, does not show significant changes in the swelling levels. The system lowers its energy through collective motion and recrystallization after a sufficient number of penalty functions are added. These relaxation processes are found to require activation barriers which, for all of the cases explored in this study via ABC, surpass 2.0 eV. Other relaxation processes with smaller activation barriers are also found, but they do not result in significant changes in volumetric expansion. In practice, at 400 K, our temperature of interest, one would not expect these relaxations to occur. This finding suggests that most of the recrystallization of the original damage takes place within the first few nanoseconds, in a time scale that can be probed reliably with MD for our high dose rate simulations. The corrections for long time scale swelling, as determined by the swelling levels in the ABC runs before a large recrystallization step, are minimal.

4 Microscopic effects: disordered phases and amorphization

Unlike the void nucleation and growth mechanisms which are responsible for swelling at lower dose rates and high doses [4–6], the mechanism responsible for the swelling observed in Figures 1 and 2 is associated with the formation and partial recovery of defected or disordered regions in the lattice. The early evolution of the microstructure during irradiation is dominated by long-range athermal interactions between the SIAs [8] which result in rapid formation of SIA clusters and localized disordered areas. Figures 3–5 show the underlying defect cluster distribution and radial distribution function (averaged over both the original and the implanted iron atoms) for runs 1 (low dose, low dose rate), 3 (low dose, medium dose rate), and 7 (high dose, high dose rate). A set of atoms is considered to comprise a defect "cluster" if and only if each atom is a nearest neighbor to at least one other atom in the group (connectedness), and each atom has a coordination number different from that of a perfect lattice (defectiveness). As can be seen in all three figures, the evolution of the macroscopic swelling under each of the irradiation conditions directly correlates with the number of miscoordinated atoms in the lattice and the size of the largest cluster. The overexpansion is directly related to the amount of disorder in the lattice; as high disorder regions create excessive local stresses, the lattice relaxes by expanding. The presence of these lower density defect zones destroys some of the short and long range order in the lattice (Figs. 3–5b).

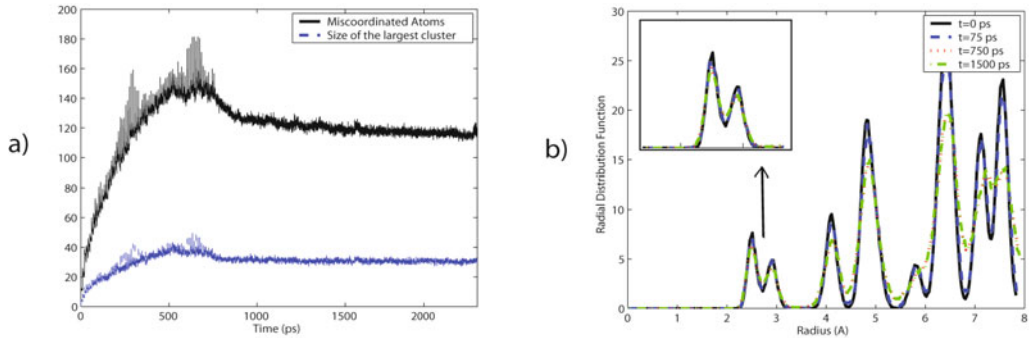

Fig. 3. Microstructural evolution of SIA-implanted Fe (run 1): (a) total amount of disorder (number of miscoordinated atoms) and the size of the largest defect cluster. (b) Radial distribution function (averaged over all iron atoms) as a function of time.

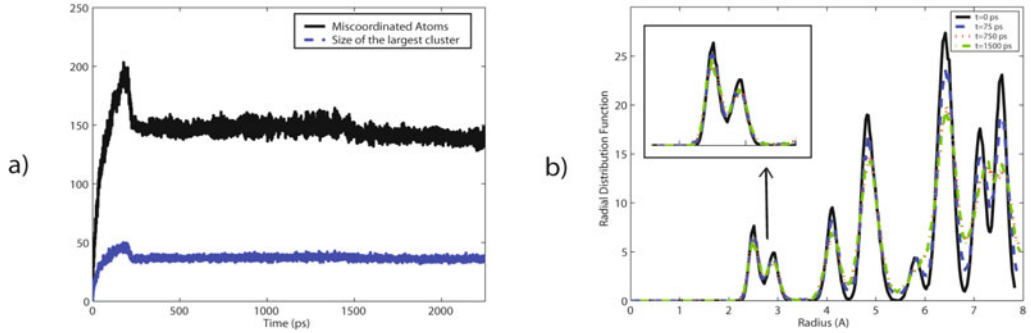

Fig. 4. Microstructural evolution of SIA-implanted Fe (run 3): (a) total amount of disorder (number of miscoordinated atoms) and the size of the largest defect cluster. (b) Radial distribution function (averaged over all iron atoms) as a function of time.

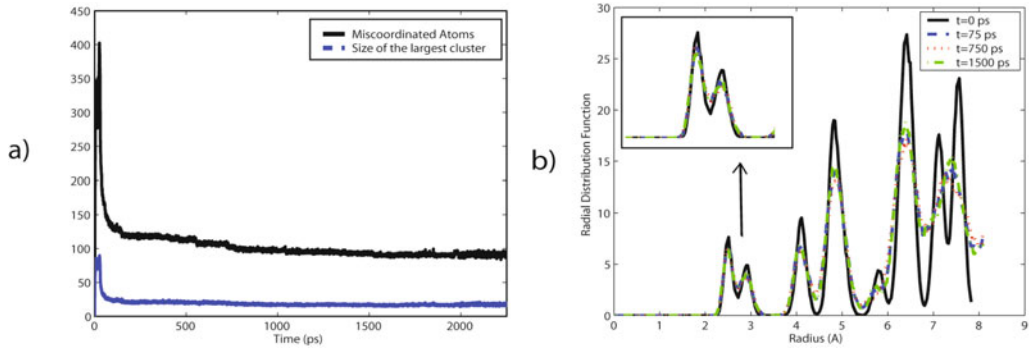

Fig. 5. Microstructural evolution of SIA-implanted Fe (run 5): (a) total amount of disorder (number of miscoordinated atoms) and the size of the largest defect cluster. (b) Radial distribution function (averaged over all iron atoms) as a function of time.

Two main driving forces determine the evolution during irradiation. As more atoms are introduced, the SIA clusters grow in size and complexity. However, as the lattice relaxes and the volume increases, there is also a strong thermodynamic driving force for recrystallization – at 400 K, the stable phase of Fe is crystalline – and, therefore, the excess atoms in small SIA clusters rearrange themselves into new lattice planes in a manner similar to that described by Hsieh and Yip [10]. The competition between these two forces gives rise to interplay of disorder creation (damage) and recovery in determining the irradiated microstructure and its evolution. The nature of the damage creation and recrystallization processes can be observed in the changes in the radial distribution function of Figures 3–5b. As damage is introduced during the early stages of irradiation (stage I), the system loses some of its long range order, resulting in the disappearance of some of the higher order peaks as well as the reduction of height in the short range ones.

Even though the total amount of disorder added to the system is the main driver of macroscopic swelling (not strongly dose rate dependent), the recovery mechanisms are expected to be more sensitive to the precise irradiation and metallurgical conditions. Differences in the underlying microstructure and their interactions with large amounts of SIAs give rise to the differences in the swelling levels described in the previous section.

Based on our findings on behavior under high dose rate conditions, we suggest three distinct microstructural features can be identified: (1) SIA clusters which relax in the

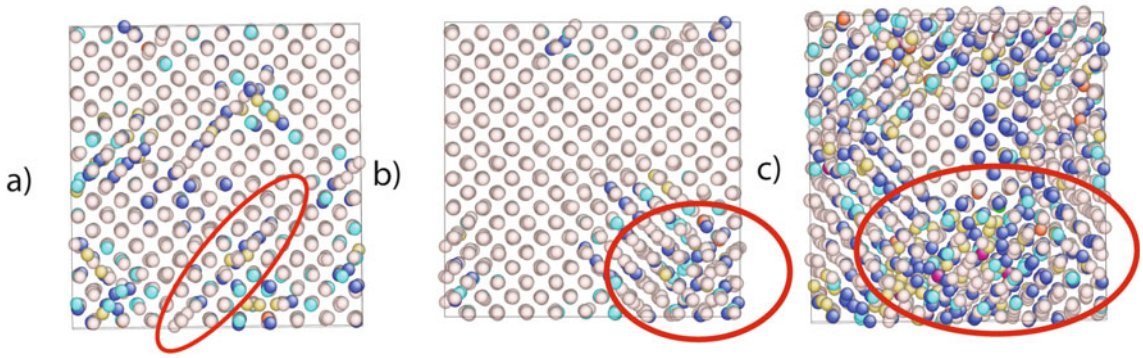

Fig. 6. Three classes of defects in SIA-implanted Fe at high dose rates: (a) SIA clusters/prismatic dislocation loops (run 1), (b) small clusters of disorder (run 3), (c) large amorphous pockets (run 7). The atoms are colored according to their coordination number. Visualizations created using AtomEye [21].

[111] direction as dislocation loops, (2) small (5–10 atoms) pockets of disorder that eventually relax into dislocation loops or recrystallize, and (3) larger regions of amorphous Fe. Figure 6 shows examples of these types of defects as they form during the microstructural evolution in runs 1, 3, and 7. During stage I, while the material is under irradiation and swelling increases to a maximum level, SIA clusters coalesce into small pockets of amorphous phases for all of the irradiation conditions explored. In this early irradiation regime, the number and average size of the defect clusters increases with the total dose. Although the rate of increase is not directly proportional to the dose rate (as can be seen from the initial slopes of the curves in Figures 1 and 3–5), deviation from this trend is not pronounced. This implies that, on average, the microstructure does not relax sufficiently quickly during stage I and, therefore, the effect of recovery is minor compared to damage creation. After irradiation stops (stage II), the defect microstructure formed during irradiation begins to undergo a more extensive process of relaxation and recrystallization. SIA atoms and small clusters quickly coalesce during and after irradiation due to their low migration energy barriers. Furthermore, they rapidly transform into small prismatic dislocation loops (Fig. 6a), which glide rapidly along lattice planes and are highly stable. On the other hand, small disorder pockets (Fig. 6b) are very unstable and relax into small SIA clusters or simply recrystallize as the lattice expands to accommodate them. Finally, sufficiently large amorphous zones (Fig. 6c) are also long-lived since they give rise to effective surfaces which need to be eliminated during recrystallization. However, despite being otherwise metastable, large amorphous regions are prone to partial recrystallization during irradiation because newly inserted SIAs, which bind to an amorphous phase (especially during the latter stages of stage I) can act as crystal nucleation sites inside the amorphous pockets.

Figure 7 shows the average coordination number (including first and second neighbor shells) of the displaced atoms for runs 1, 3, and 5. The intermediate dose rate (run 3) is characterized by small changes in coordination (from a perfect bcc coordination of 14–8 nearest neighbors

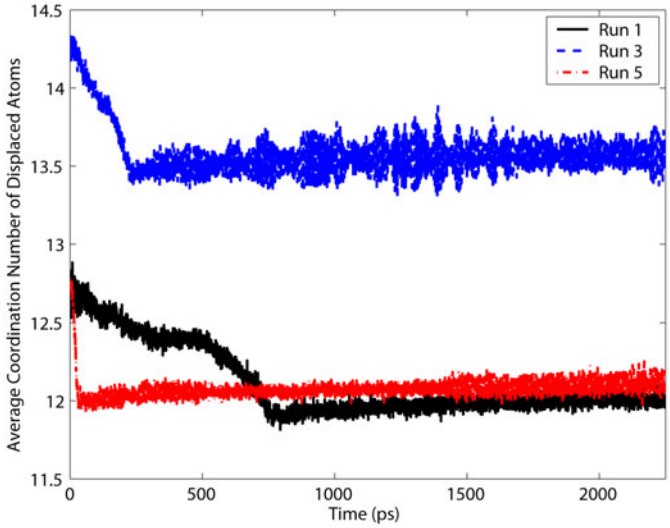

Fig. 7. Average coordination number of the displaced atoms for runs 1, 3, and 5 after the first 1 ps. Perfectly coordinated atoms have 14 first and second nearest neighbors.

and 6 second nearest neighbors – to about 13.5), while at high and low dose rates we observe more dramatic changes (a reduction of the coordination of the defected atoms to about 12), which are stationary in time. At dose rates below 10^8 dpa/s, newly implanted SIAs can relax to dumbbell positions, migrate, and form clusters. These clusters relax into the equilibrium mobile configuration in the [111] direction in the form of small prismatic dislocation loops which migrate through the lattice. As these defects are stable there is little swelling recovery in the long run relative to that which takes place shortly after irradiation, so the resulting miscoordination is not only more drastic, as all of the dislocation loops have a similar low coordination configuration, but also more persistent.

In contrast, intermediate dose rates are characterized by a combination of SIA clusters and small pockets of disorder. As discussed earlier, these configurations are highly unstable so they recrystallize quickly during both stages I and II, and consequentially the average decrease in coordination is smaller and less persistent. This leads to a

lower level of swelling for the same dose. At higher dose rates, the size of the disorder pockets grows until some of them become metastable regions of amorphous material. By reaching a critical size or turning into dislocation loops these large pockets lower the average coordination of the lattice sufficiently (Fig. 7) to avoid complete recrystallization. Additionally, at higher doses, newly implanted SIAs are observed to act as nucleation sites inside amorphous regions and foster recrystallization of the larger pockets, thus explaining the sharp recovery observed at high total doses.

Because of the high dose rates analyzed in this study, direct comparison with experimental results on irradiated samples of bulk bcc Fe is, to our knowledge, not yet feasible. Experimental studies of focused ion beam implantation in MgO surfaces [22] do show swelling behavior with macroscopic and microscopic features that can be compared with the observations in this study. After ion beam irradiation, the MgO surfaces expand outwardly (swelling) and then as the microstructure evolves the surface recovers and contracts into the material. The swelling behavior in Rota's study [22] is the result of the evolution of a disordered microstructure created during irradiation consisting of defected clusters, partial amorphization, and other morphological changes in the multilayer arrangement. These surface results provide some support for an alternative swelling mechanism driven primarily by morphological rearrangement and SIA-driven amorphization, which we believe is consistent with our findings which do not explicitly involve vacancy accumulation as the mechanism for swelling.

5 Summary

In this paper, we probed the mechanisms of SIA-driven swelling in Fe at high dose rates by a combination of MD and transition state pathway sampling simulations. We have uncovered a swelling mechanism associated with the formation, recovery, and survival of pockets of disordered phases that result from competing processes of damage creation due to irradiation and the strong long-range interactions between SIAs leading to recrystallization. We have identified three regimes of microstructural evolution characterized by SIA clusters which transform into dislocation loops, small pockets of disorder that either evolve into dislocation loops or recrystallize, and larger regions of amorphous Fe. These regimes are responsible for a non-monotonic variation of swelling with dose rate as a result of the interplay between stability and evolving structural distortions associated with each microstructural defect type. We also provide the first indication that microstructural features revealed by MD simulations may survive to much longer times. Our results have motivated us to attempt simulations of more realistic dose rates with full atomistic resolution during irradiation. For that subsequent study, we have developed an extension of the ABC method to sample a dynamic energy landscape (as opposed to a static landscape) [14], work which will be presented in a future publication.

We benefited from computational resources funded by the US National Science Foundation (DMR-0414849) and Corning Incorporated.

References

1. L.K. Mansur, J. Nucl. Mat. **216**, 97 (1994)
2. M.T. Robinson, J. Nucl. Mat. **216**, 1 (1994)
3. C. Cawthorne, E. Fulton, Nature **216**, 575 (1967)
4. F.A. Garner, W.G. Wolfer, J. Nucl. Mat. **122-123**, 201 (1984)
5. T. Okita, T. Sato, N. Sekimura, F.A. Garner, L.R. Greenwood, J. Nucl. Mat. **307**, 322 (2002)
6. M.P. Surh, J.B. Sturgeon, W.G. Wolfer, J. Nucl. Mat. **378**, 86 (2008)
7. A. Vehanen et al., Phys. Rev. B **26**, 762 (1982)
8. Y. Limoge, A. Barbu, Phys. Rev. B **30**, 2212 (1984)
9. J. Nord, K. Nordlund, J. Keikonen, Phys. Rev. B **65**, 165329 (2002)
10. H. Hsieh, S. Yip, Phys. Rev. Lett. **59**, 2760 (1987)
11. M.J. Caturla, T. Diaz de la Rubia, G. Gilmer, J. Appl. Phys. **77**, 3120 (1995)
12. A. Kushima et al., J. Chem. Phys. **130**, 224504 (2009)
13. Y. Fan, A. Kushima, B. Yildiz, Phys. Rev. B **81**, 104102 (2010)
14. P.R. Monasterio Velasquez, Ph.D. thesis, Massachusetts Institute of Technology, 2010
15. G.J. Ackland, M.I. Mendelev, D.J. Srolovitz, S.W. Han, A.V. Barashev, J. Phys.: Condens. Matter **16**, S2629 (2004)
16. D.S. Gelles, J. Nucl. Mat. **225**, 163 (1995)
17. Y. Limoge, A. Rahman, H. Hsieh, S. Yip, J. Non-Cryst. Sol. **99**, 75 (1988)
18. A. Laio, M. Parrinello, Proc. Natl. Acad. Sci. **99**, 12562 (2002)
19. A. Laio, F.L. Gervasio, Rep. Prog. Phys. **71**, 126601 (2008)
20. M.P. Surh, J.B. Sturgeon, W.G. Wolfer, J. Nucl. Mat. **328**, 107 (2004)
21. J. Li, Modelling Simul. Mater. Sci. Eng. **11**, 173 (2003)
22. A. Rota et al., Surf. Sci. **600**, 3718 (2006)